Journal of *Marine Science and Engineering*

MDPI

Article

Compact Impedance Matching Circuit for Wideband Power Transfer in Janus Helmholtz Transducers

Kibae Lee [1], Hyun Hee Yim [1], Yoonsang Jeong [1], Jongkil Lee [2] and Chong Hyun Lee [1,*]

[1] Department of Ocean System Engineering, Jeju National University, Jeju 63243, Republic of Korea; kibae0211@stu.jejunu.ac.kr (K.L.); hyhyun0817@stu.jejunu.ac.kr (H.H.Y.); jyssolt@stu.jejunu.ac.kr (Y.J.)
[2] Department of Mechanical Engineering Education, Gyeongkuk National University, Andong 36729, Republic of Korea; jlee@anu.ac.kr
* Correspondence: chonglee@jejunu.ac.kr; Tel.: +82-64-754-3481

Abstract: The Janus Helmholtz transducer (JHT) is known for high transmission voltage response (TVR) over a wide bandwidth by its dual-resonance characteristics. It is usually required to design matching circuits for wideband power transmission of JHT. However, conventional matching circuit designs can neither easily cover wide bandwidth nor deliver maximum active power to load. To address this limitation, we propose a novel impedance matching circuit design method to maximize overall power transfer efficiency. The method is based on objective functions of both input and load power factors. The proposed method achieves better active power transfer to load than methods using commonly used input power factor alone. To prove feasibility of the proposed method, we consider equivalent circuit models of cable and JHT and adopt a compact matching circuit of resonant components and a coupling capacitor. By considering three JHTs, two power driving systems, and two frequency bands, we show that the proposed method can achieve a significant improvement in active power transfer to load. By conducting experiments of equivalent JHT circuit, cable, and matching circuit, we also show that input power factor increases by 73.2%, while active power delivered to load increases by 2.03 mW with 1 V_{rms} input voltage.

Keywords: Janus Helmholtz transducer; impedance matching circuit; wideband power transfer

check for updates

Academic Editor: Erkan Oterkus

Received: 13 March 2025
Revised: 20 April 2025
Accepted: 29 April 2025
Published: 30 April 2025

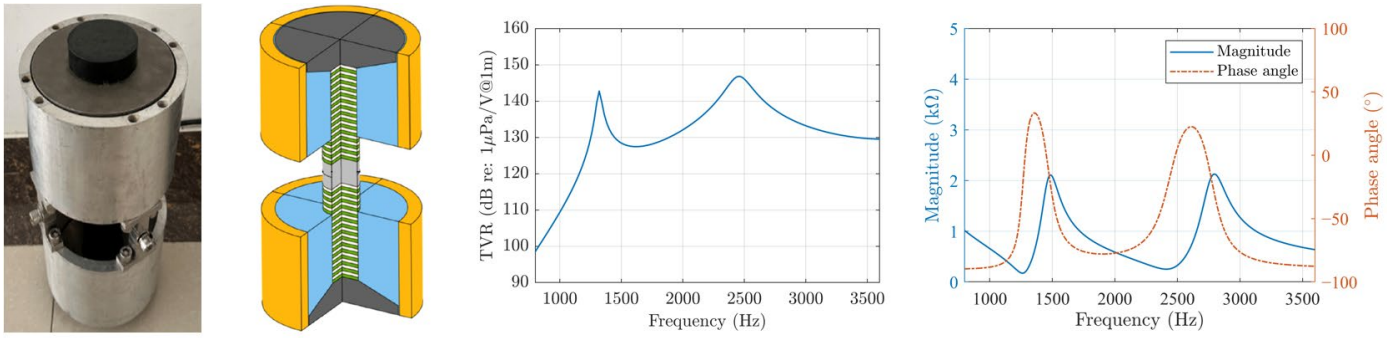
Citation: Lee, K.; Yim, H.H.; Jeong, Y.; Lee, J.; Lee, C.H. Compact Impedance Matching Circuit for Wideband Power Transfer in Janus Helmholtz Transducers. *J. Mar. Sci. Eng.* **2025**, *13*, 898. https://doi.org/10.3390/jmse13050898

Copyright: © 2025 by the authors. Licensee MDPI, Basel, Switzerland. This article is an open access article distributed under the terms and conditions of the Creative Commons Attribution (CC BY) license (https://creativecommons.org/licenses/by/4.0/).

1. Introduction

The demand for underwater transducers with low-frequency, wideband, and high-power characteristics has been increasing in various fields, including marine environmental monitoring, deep-sea exploration and sonar surveillance systems [1–5]. To address these demands, various transducers have been studied, among which the Janus Helmholtz transducer (JHT) has gained attention for its simultaneous wideband and high-power characteristics [6–9]. The JHT consists of two symmetrically arranged Tonpilz transducers and a cylindrical metal housing, as shown in Figure 1. This structure utilizes both the longitudinal resonance of the transducers and the cavity resonance of the fluid, providing a high transmission voltage response (TVR) over a wide bandwidth. The TVR represents the transmission performance of the JHT and is defined as the sound pressure level radiated into the medium per unit input voltage, typically measured under 1 V_{rms} excitation. Despite these advantages, the JHT has a large phase difference between voltage and current at most frequencies, except for its resonance frequencies. This phase difference increases the reactive power, restricting high-power transmission. For instance, as shown in Figure 1, although the TVR remains at a usable level above 127 dB between the two resonances of

the JHT, the phase difference between voltage and current reaches up to 77.8°, making wideband power transfer difficult.



(a) (b) (c) (d)

Figure 1. A JHT example: (**a**) photograph [8], (**b**) geometry, (**c**) TVR and (**d**) impedance characteristics.

An impedance matching circuit can be utilized to address this issue. Existing impedance matching circuits are typically designed either to correct the phase difference between voltage and current using resonant circuits or to compensate for the capacitance of the transducer using the secondary inductance of a transformer [10–14]. These circuits are generally designed to maximize the power factor at the input impedance, which includes the transducer. The power factor is an index that quantifies the phase difference between voltage and current and reflects the efficiency of power transfer. In such designs, the values of passive components are typically determined either by experimental tuning or by employing optimization algorithms. These methods, however, match impedance only within the resonance frequency band, limiting their applicability to the JHT, which operates in non-resonant frequency bands. Additionally, these methods often include inductors or transformers with high inductance, leading to increased physical size and higher manufacturing costs.

Similar to the JHT, studies on impedance matching for transducers with dual resonance characteristics are also being conducted [15]. This study combines different resonance circuits to achieve impedance matching at dual frequencies. In this design, different resonant circuits are simply connected in sequence. The component values are adjusted experimentally so that the sound pressure reflected from the reflector is maximized at the two resonant frequencies. This circuit, however, is only applicable at the resonant frequencies of the transducer. Furthermore, the interactions between different resonance circuits are not considered in the design process, limiting its ability to achieve wideband impedance matching.

Recent studies have focused on incorporating active components to improve the bandwidth limitations of conventional impedance matching circuits [16,17]. These studies enhance wideband power efficiency by controlling the phase of the input voltage. The impedance matching circuit based on active components typically consists of switching elements that adjust the phase of the voltage. These circuits adjust the voltage phase to align with the current phase at the input impedance. These circuits, however, require complex and precise control logic, along with additional measurement devices, to adapt to the nonlinear load characteristics of the transducer.

This paper proposes an impedance matching circuit with simple structure to enable wideband power transfer in the JHT. The proposed matching circuit integrates two resonant circuits composed of inductors and capacitors. This circuit is designed to maximize the power factors of both the input and load. The design process consists of two main steps. First, the input and load impedance of the circuit are calculated within the driving system.

Subsequently, an optimization algorithm is used to determine the circuit component values, maximizing the power factors over the operating frequency range. The circuit designed in this manner is validated through simulations and experiments for its power transfer performance in the JHT.

Our paper is organized as follows: Section 2 describes the structure of the proposed impedance matching circuit, the impedance analysis method and the circuit design process. In Section 3, simulation results for the JHTs with various characteristics are described and power transfer performance of the designed circuit is demonstrated. Section 4 provides experimental results obtained by using an equivalent JHT circuit model and demonstrate improvements in both input power factor and the active power delivered to the load. Conclusions are presented in Section 5.

2. Impedance Matching Circuit

Figure 2 illustrates two power driving circuit diagrams for JHT, which include an impedance matching circuit, cable and input source. The impedance matching circuit consists of two resonant circuits, each composed of an inductor L and a capacitor C, which are interconnected through a coupling capacitor C_m [18,19]. Note that the placement of the matching circuit is different. In Case I, the impedance matching circuit is placed between the voltage source and the cable, while it is located between the cable and the JHT in Case II. For modeling the cable, we adopt the cable equivalent circuit of cable length ℓ, the per-unit-length resistance R_c, inductance L_c, capacitance C_c and conductance G_c [12,20].

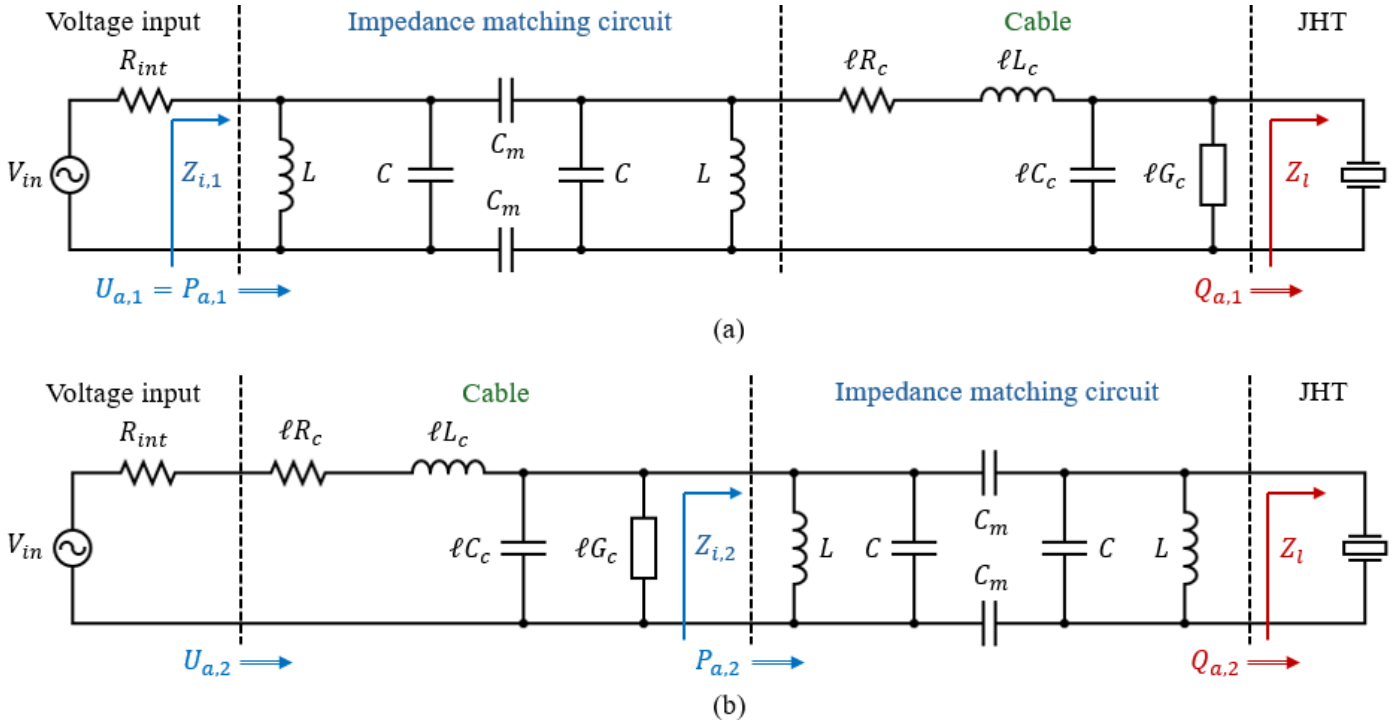


Figure 2. Two driving circuit diagrams. (**a**) Case I: Impedance matching circuit placed between voltage input and cable. (**b**) Case II: Impedance matching circuit placed between the cable and the JHT.

We rearrange the circuits in Figure 2 into equivalent impedance circuits as shown in Figure 3. The obtained equivalent circuits consist of six meshes and their currents $I_{k,\,n}$, $n \in \{1,\,2,\,\cdots,\,6\}$, where $k \in \{1,\,2\}$ represents Case I and II. Note that the internal resistance in voltage source is denoted as R_{int} and load impedance representing the JHT impedance as Z_l. The series and parallel impedances of cable are given by $Z_{sc} = \ell(R_c + j2\pi f L_c)$ and

$Z_{pc} = 1/(\ell G_c + j2\pi f \ell C_c)$, where impedances of L, C and C_m are expressed as $Z_L = j2\pi fL$, $Z_C = 1/j2\pi fC$ and $Z_{C_m} = 1/j2\pi fC_m$, respectively.

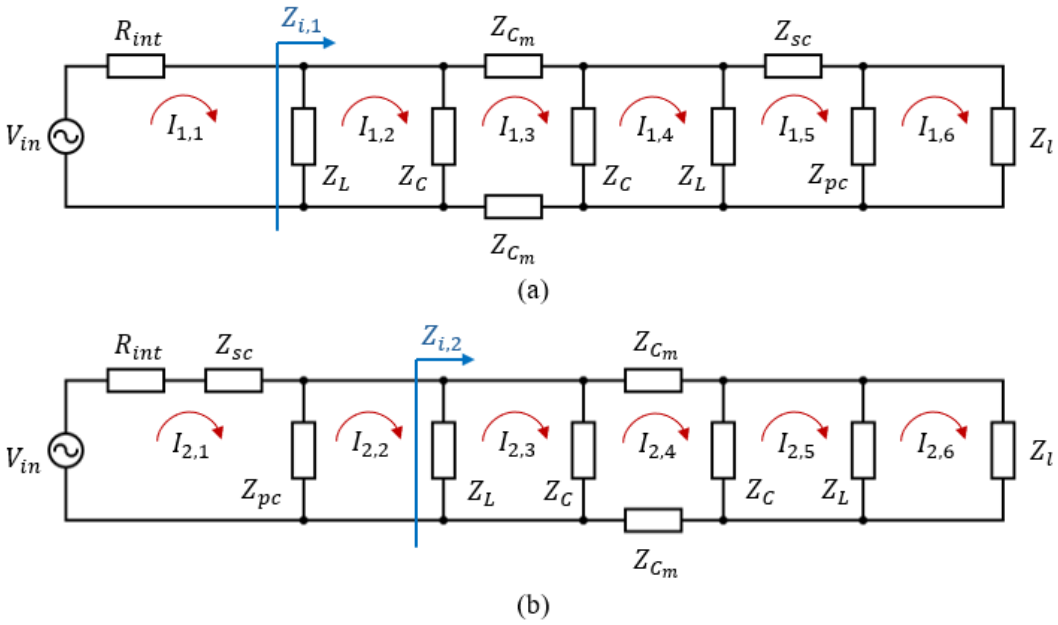


Figure 3. Equivalent impedance circuit diagram: (**a**) Case I and (**b**) Case II.

2.1. Impedances of the Driving System

The input impedance $Z_{i,1}$ of Case I can be obtained by combining impedances of the matching circuit, the cable and the JHT as follows:

$$Z_{i,1} = Z_L \parallel Z_C \parallel \left(2Z_{Cm} + Z_C \parallel Z_L \parallel \left(Z_{sc} + \left(Z_{pc} \parallel Z_l\right)\right)\right) \tag{1}$$

The complex impedances of $Z_{i,1}$ and Z_l are composed of resistance R and reactance X so that they can be expressed as $Z_{i,1} = R_{i,1} + jX_{i,1}$ and $Z_l = R_l + jX_l$. Subsequently, by applying Kirchhoff's voltage law (KVL) [21], all loop equations can be expressed as equation of $\widetilde{V}_1 = \widetilde{Z}_1 \widetilde{I}_1$, where $\widetilde{V}_1 = [V_{in},\ 0,\ 0,\ 0,\ 0,\ 0]^{\mathrm{T}}$, $\widetilde{I}_1 = [I_{1,1},\ I_{1,2},\ I_{1,3},\ I_{1,4},\ I_{1,5},\ I_{1,6}]^{\mathrm{T}}$ and the impedance matrix $\widetilde{Z}_1$ becomes as follows:

$$\widetilde{Z}_1 = \begin{bmatrix} R_{int} + Z_L & -Z_L & 0 & 0 & 0 & 0 \\ -Z_L & Z_{LC} & -Z_C & 0 & 0 & 0 \\ 0 & -Z_C & 2Z_{CC_m} & -Z_C & 0 & 0 \\ 0 & 0 & -Z_C & Z_{LC} & -Z_L & 0 \\ 0 & 0 & 0 & -Z_L & Z_L + Z_{spc} & -Z_{pc} \\ 0 & 0 & 0 & 0 & -Z_{pc} & Z_{pc} + Z_l \end{bmatrix} \tag{2}$$

where $Z_{LC} = Z_L + Z_C$, $Z_{CC_m} = Z_C + Z_{C_m}$ and $Z_{spc} = Z_{sc} + Z_{pc}$. The current from input current $I_{i,1} = I_{1,1}$ to load current $I_{l,1} = I_{1,6}$ can be obtained by $\widetilde{I}_1 = \widetilde{Z}_1^{-1} \widetilde{V}_1$ and they are expressed as Equations (A1)–(A6) in Appendix A.

Source voltage $V_{s,2}$ and impedance $Z_{s,2}$ of Case II can be determined by using Thevenin's theorem [21] and expressed as follows:

$$V_{s,2} = \frac{V_{in} Z_{pc}}{R_{int} + Z_{spc}} \tag{3}$$

$$Z_{s,2} = \frac{(R_{int} + Z_{sc})Z_{pc}}{R_{int} + Z_{spc}} \tag{4}$$

Similarly, the input impedance $Z_{i,2}$ can expressed as follows:

$$Z_{i,2} = Z_L \parallel Z_C \parallel (2Z_{Cm} + Z_C \parallel Z_L \parallel Z_l) \tag{5}$$

The complex impedances of $Z_{s,2}$ and $Z_{i,2}$ are represented as $Z_{s,2} = R_{s,2} + jX_{s,2}$ and $Z_{i,2} = R_{i,2} + jX_{i,2}$, respectively. The loop equations are also expressed as $\widetilde{V}_2 = \widetilde{Z}_2 \widetilde{I}_2$, where $\widetilde{V}_2 = [V_{s,2},\ 0,\ 0,\ 0,\ 0,\ 0]^{\mathrm{T}}$, $\widetilde{I}_1 = [I_{2,1},\ I_{2,2},\ I_{2,3},\ I_{2,4},\ I_{2,5},\ I_{2,6}]^{\mathrm{T}}$ and the impedance matrix $\widetilde{Z}_2$ becomes as follows:

$$\widetilde{Z}_2 = \begin{bmatrix} R_{int} + Z_{spc} & -Z_{pc} & 0 & 0 & 0 & 0 \\ -Z_{pc} & Z_{pc} + Z_L & -Z_L & 0 & 0 & 0 \\ 0 & -Z_L & Z_{LC} & -Z_C & 0 & 0 \\ 0 & 0 & -Z_C & 2Z_{CC_m} & -Z_C & 0 \\ 0 & 0 & 0 & -Z_C & Z_{LC} & -Z_L \\ 0 & 0 & 0 & 0 & -Z_L & Z_L + Z_l \end{bmatrix} \tag{6}$$

Similarly, the loop currents in Case II are obtained by the equation $\widetilde{I}_2 = \widetilde{Z}_2^{-1} \widetilde{V}_2$, and are expressed as Equations (A7)–(A12) in Appendix A. Here, the input current is $I_{i,2} = I_{2,2}$, and the load current is $I_{l,2} = I_{2,6}$.

2.2. Design of the Impedance Matching Circuit

The source impedance of Case I consists only of resistance R_{int} so that the input current $I_{i,1}(\phi,\ f)$ can be expressed as follows:

$$I_{i,1}(\phi,\ f) = \frac{V_{in}}{R_{int} + R_{i,1}(\phi, f) + jX_{i,1}(\phi,\ f)} \tag{7}$$

where $\phi \in \{L,\ C,\ C_m\}$ denotes a design parameter of the matching circuit. Then, the active power at the input of the matching circuit $P_{a,1}(\phi,\ f)$, can be expressed as follows:

$$P_{a,1}(\phi,\ f) = |I_{i,1}(\phi,\ f)|^2 R_{i,1}(\phi, f) = \frac{V_{in}^2 R_{i,1}(\phi, f)}{(R_{int} + R_{i,1}(\phi, f))^2 + X_{i,1}^2(\phi,\ f)} \tag{8}$$

To maximize $P_{a,1}(\phi,\ f)$, $R_{i,1}(\phi, f)$ and R_{int} must match and $X_{i,1}(\phi,\ f)$ should be minimized. Since $P_{a,1}(\phi,\ f)$ is an unbounded non-negative value, we define the input power factor $\eta_1(\phi,\ f)$ as the ratio of $P_{a,1}(\phi,\ f)$ to the input power $P_{i,1}(\phi,\ f)$ for normalization purposes. The input power $P_{i,1}(\phi,\ f)$ can be expressed as follows:

$$P_{i,1}(\phi,\ f) = |I_{i,1}(\phi,\ f)|^2 \sqrt{R_{i,1}^2(\phi, f) + X_{i,1}^2(\phi,\ f)} \tag{9}$$

Then, the input power factor $\eta_1(\phi,\ f)$ to be maximized can be expressed as follows:

$$\eta_1(\phi,\ f) = \frac{P_{a,1}(\phi,\ f)}{P_{i,1}(\phi,\ f)} = \frac{1}{\sqrt{1 + (X_{i,1}(\phi,\ f)/R_{i,1}(\phi, f))^2}} \tag{10}$$

Note that the $\eta_1(\phi,\ f)$ is bounded as $0 \le \eta_1(\phi,\ f) \le 1$. Similar to the condition for maximizing $P_{a,1}(\phi,\ f)$, maximizing $\eta_1(\phi,\ f)$ becomes minimizing $X_{i,1}(\phi,\ f)/R_{i,1}(\phi, f)$. Note $\eta_1(\phi,\ f)$ becomes 1 as $R_{i,1}(\phi, f)$ increases to infinity. However, $\eta_1(\phi,\ f)$ close to 1 does not guarantee actual effective power transfer to load, and we adopt load power factor

$\psi(f)$ quantifying the efficiency of power transfer to the load. For $\psi(f)$, we define the active power delivered to the load $Q_{a,1}(\phi, f)$ and total load power $Q_{l,1}(\phi, f)$ as follows:

$$Q_{a,1}(\phi, f) = \left|I_{l,1}(\phi, f)\right|^2 R_l(f) \tag{11}$$

$$Q_{l,1}(\phi, f) = \left|I_{l,1}(\phi, f)\right|^2 \sqrt{R_l^2(f) + X_l^2(f)} \tag{12}$$

Then, the $\psi(f)$, i.e., the ratio of $Q_{a,1}(\phi, f)$ to $Q_{l,1}(\phi, f)$, can be expressed as follows:

$$\psi(f) = \frac{Q_{a,1}(\phi, f)}{Q_{l,1}(\phi, f)} = \frac{1}{\sqrt{1 + (X_l(f)/R_l(f))^2}} \tag{13}$$

Note that the $\psi(f)$ is bounded as $0 \leq \psi(f) \leq 1$. The expressions for input power factor $\eta_2(\phi,\ f)$ and the load power factor $\psi(f)$ in Case II are presented in Appendix B. Note that $\psi(f)$ of Case II is identical to that of Case I.

By combining both $\eta_k(\phi,\ f)$ and $\psi(f)$, we finally propose two kinds objective functions to determine L and C_m in the matching circuit. By maximizing these functions over the operating frequency range f_{drive}, the L and C_m can be found by maximizing functions as follows:

$$\underset{L,\, C_m}{\arg\max} \sum_{f \in f_{drive}} (1-\lambda) \cdot \eta_k(\phi,\ f) + \lambda \cdot \psi(f) \tag{14}$$

$$\underset{L,\, C_m}{\arg\max} \sum_{f \in f_{drive}} (1-\lambda) \cdot \log \eta_k(\phi, f) + \lambda \cdot \log \psi(f) \tag{15}$$

where $0 \leq \lambda < 1$ and C coupled with L is a fixed small value.

By controlling λ, we can adjust the contribution of $\eta_k(\phi,\ f)$ and $\psi(f)$. A small λ places more emphasis $\eta_k(\phi,\ f)$, reducing reactance of the input impedance while big λ increases the contribution of $\psi(f)$, promoting power delivery to the load. Since $\psi(f)$ depends only on frequency not ϕ, it acts as regularization term giving consistent power transfer on an overall frequency band. By virtue of $\psi(f)$, we can obtain ϕ maximizing $Q_{a,1}(\phi, f)$, while preventing extremely big $R_{i,1}(\phi, f)$ or making $\eta_k(\phi,\ f)$ close to 1.

To obtain the optimum values of L and C_m, we adopt the particle swarm optimization (PSO) algorithm [22]. The PSO algorithm optimizes candidate solutions, known as particles, through an iterative process. Each particle updates its position by considering the best solutions found by neighboring particles in a predefined range. The PSO algorithm is well suited for exploring non-convex and non-smooth design spaces. Unlike gradient-based methods, the PSO algorithm does not require derivative computation, which is difficult to obtain in the complex domain. Furthermore, the PSO algorithm requires fewer control parameters compared to the genetic algorithm. In the PSO algorithm, each particle representing a candidate set of L and C_m is updated at each iteration, and then input impedance is computed to evaluate the $\eta_k(\phi, f)$ by using the updated values.

To compare ours with existing impedance matching methods, we present a table of summary in Table 1. Passive circuits are simple and easy to implement, but they are only useful for narrow bandwidth [10,11], while active circuits provide very wide bandwidth but require complex control and external devices [16,17]. However, the proposed two-resonant circuit can handle not only wide bandwidth without external devices, but retaining low design complexity.

Table 1. Comparison of impedance matching circuits for underwater transducer.

Category	Passive Circuit [10,11]	Active Circuit [16,17]	Two-Resonant Circuit
Bandwidth	Narrow	Very wide	Wide
Design complexity	Low	High	Low
Implementation complexity	Low	High	Low
External device	Not required	Required	Not required

3. Simulation Results

3.1. Design Details of the JHT and the Impedance Matching Circuit

We utilize the distributed parameter model (DPM) [8], shown in Figure A1 in Appendix C, to design the JHT and obtain its impedance characteristics. The axisymmetric model is shown in Figure 4, and structural parameters of the designed JHT are listed in Table 2. Additionally, material properties of the JHT are listed in Table A1 in Appendix C. Note that the Type I is identical to the JHT in Ref. [8], while the Type II and III are designed to exhibit low-frequency characteristics similar to that in Ref. [6]. Additionally, the cable is modeled to exhibit electrical characteristics equivalent to that in Ref. [12] for a length of 100 m, as presented in Table A2 in Appendix C.

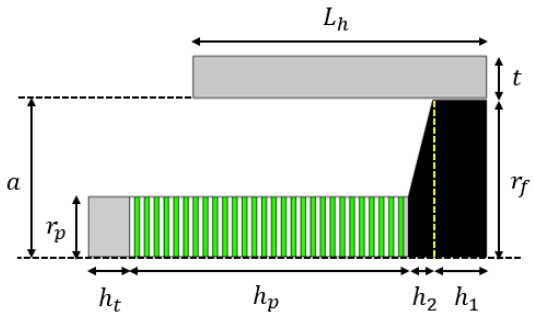


Figure 4. Two-dimensional axisymmetric diagram of the JHT.

Table 2. Structural parameters of the JHT in mm.

Structural Parameter	Type I [8]	Type II	Type III
Thickness of the tail mass (h_t)	20	42	42
Radius of the piezoelectric disc (r_p)	28	94	61
Thickness of the piezoelectric stack (h_p)	150	767	285
Radius of the head mass (r_f)	95	160	160
Thickness of the head mass (h_1, h_2)	15, 25	55, 25	55, 25
Radius of the housing (a)	97	162	162
Thickness of the housing (t)	15	38	43
Length of the housing (L_h)	150	423	456

Figure 5 illustrates the impedance characteristics of the load. In this paper, the resonant frequencies are defined based on Z_l. The resonant frequencies are identified as the frequencies at which the phase of Z_l is closest to 0°, meaning that its reactance is minimized. These frequencies define the boundaries of a wide non-resonant band, where the phase of the load impedance notably deviates from 0°. This region can be characterized by increased reactance, which leads to a large phase difference between voltage and current and results in reduced power transfer efficiency. Note that the Type I has resonant frequencies at 1450 Hz and 2480 Hz, while the Type II has resonant frequencies at 620 Hz and 905 Hz. The Type III has wider non-resonant band than Type II, and has resonant frequencies at 545 Hz and 970 Hz.

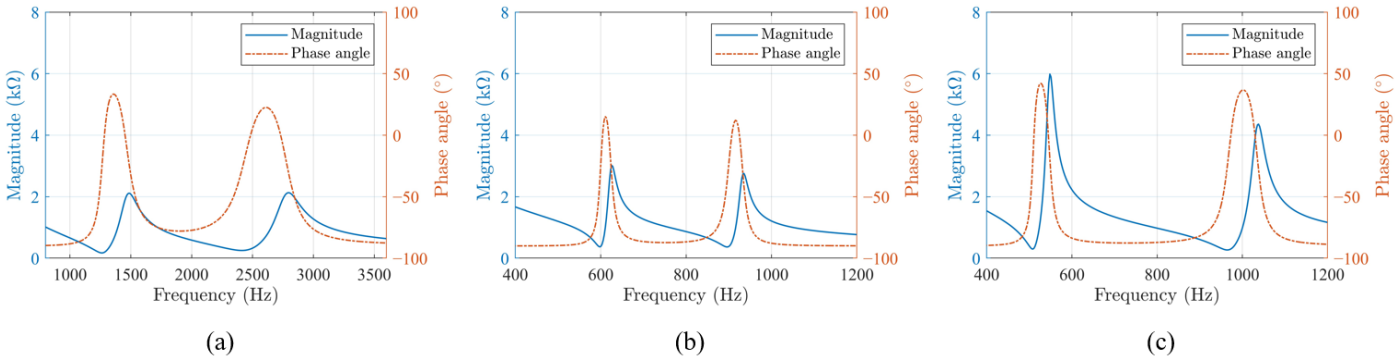


Figure 5. Impedance characteristics of the load: (**a**) Type I, (**b**) Type II and (**c**) Type III.

Usually, the JHT is used for frequency band between the two resonant frequencies. However, we consider two frequency bands illustrated in Figure 6 to evaluate performance of the proposed impedance matching circuit. The first region Δf_e covers wider frequency bands, including both resonant and intermediate non-resonant band. The second region Δf_n corresponds to only non-resonant bands, and its bandwidth is empirically set to be 60% of Δf_e. Thus, load impedance of Δf_n band has large reactance, and power transfer efficiency can be reduced. The frequency bands of three types are summarized in Table 3.

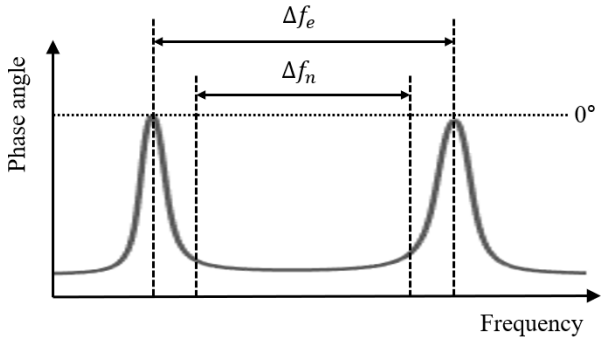


Figure 6. Band allocation for impedance matching.

Table 3. Frequency ranges and bandwidths in Hz.

Band		Type I	Type II	Type III
Δf_n	Frequency range	[1656, 2274]	[667, 848]	[630, 885]
	Bandwidth	618	181	255
Δf_e	Frequency range	[1450, 2480]	[620, 905]	[545, 970]
	Bandwidth	1030	285	425

The values of L and C_m in the impedance matching circuit are determined by the PSO algorithm using Equations (14) and (15). In this design, C is fixed at 1 pF, and R_{int} is assumed to be 50 Ω, which is typical output impedance of signal generators. To ensure practical feasibility, L is constrained within the range of 1 mH to 1000 mH, while C_m varies from 1 nF to 5000 nF. Furthermore, both L and C_m are represented as integer values in millihenries and nano-farads, respectively, without decimal precision.

In simulations, power transfer performance is evaluated by comparing the average of $\eta_k(\phi,\ f)$ with average of $Q_{a,k}(\phi,\ f)$ on the matching band. We also evaluate power transfer rate, which is defined as ratio of $Q_{a,k}(\phi,\ f)$ to active power $U_{a,k}(\phi,\ f)$ when voltage source is supplied. Then, $U_{a,1}(\phi,\ f) = P_{a,1}(\phi,\ f)$ and $U_{a,2}(\phi,\ f)$ is given as follows:

$$U_{a,2}(\phi,\ f) = |I_{2,1}(\phi,\ f)|^2 R_{tot,2}(\phi, f) \tag{16}$$

where $R_{tot,2}(\phi, f)$ denotes the resistance of the total impedance $Z_{tot,2}(\phi, f)$ excluding R_{int} in Case II, and $Z_{tot,2}(\phi, f)$ is given as follows:

$$Z_{tot,2}(\phi, f) = Z_{sc}(f) + Z_{pc}(f) \parallel Z_{i,2}(\phi, f) \tag{17}$$

By considering two power driving systems and three types of JHTs, we perform simulations in terms of power factor, active power and power transfer rate as in Figure 7. The two objective functions are evaluated by changing λ from 0 to 0.9 with 0.1 increment.

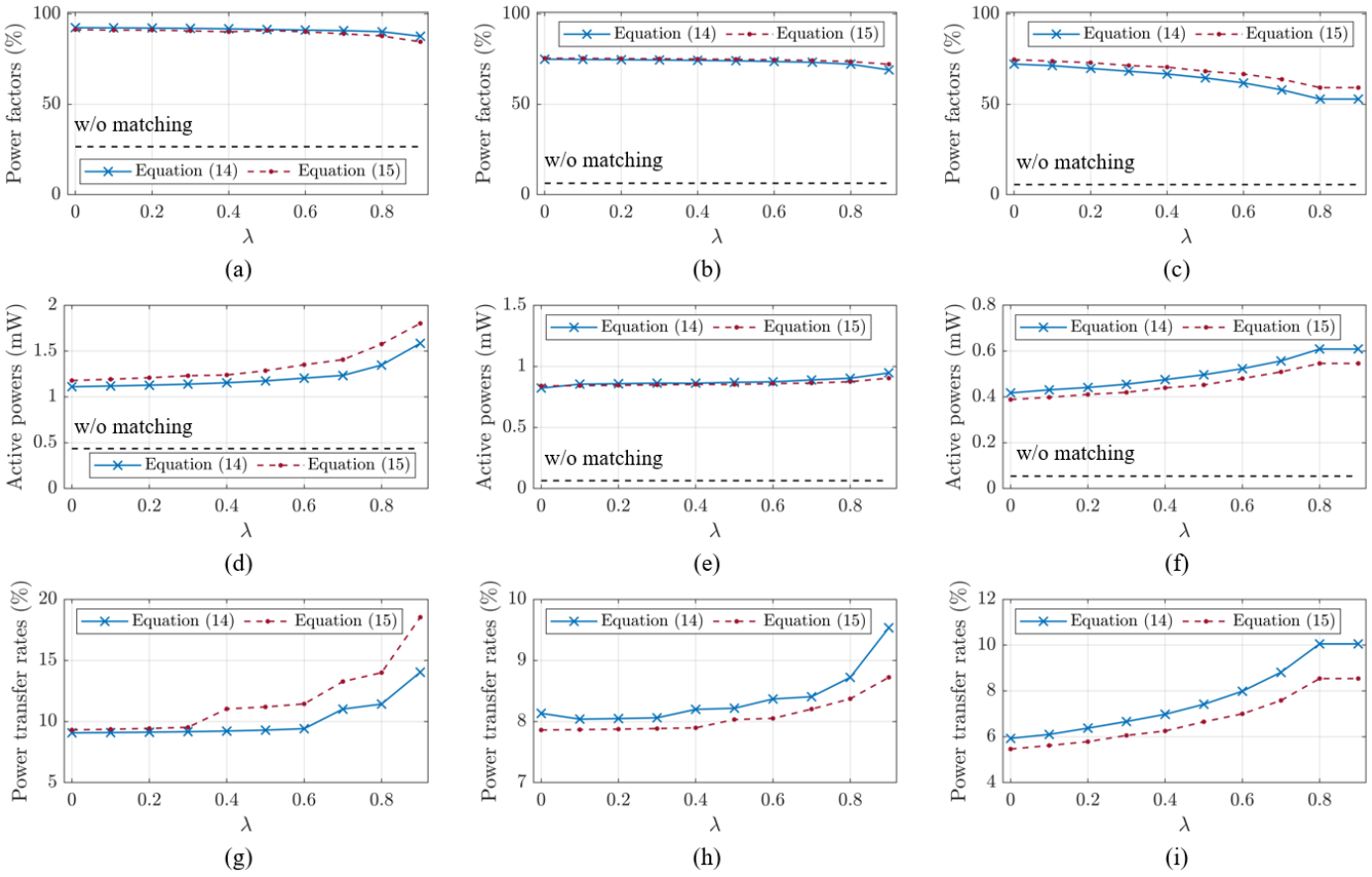


Figure 7. Changes (Type I, Type II and Type III) according to λ in the Δf_n for Case I: (**a**–**c**) the averages of input power factor, (**d**–**f**) the averages of active power delivered to the JHT and (**g**–**i**) the averages of power transfer rate to the JHT.

3.2. Evaluation of the Impedance Matching Circuit in Case I

This section presents the impedance matching circuit design for the three JHTs in Case I and evaluates the corresponding power transfer efficiencies. Table A3 in Appendix D lists the values of L and C_m determined by the two objective functions with respect to λ within Δf_n and Δf_e. Figure 7a–c shows the averages of input power factors within Δf_n, while Figure 7d–f presents the corresponding averages of active power delivered to the JHT, all calculated with 1 V_{rms} input voltage. Figure 7g–i presents the corresponding averages of power transfer rate to the JHT.

The input power factor decreases as λ increases for all JHTs and it becomes maximum when $\lambda = 0$, corresponding to circuit design by $\eta_1(\phi, f)$ only. However, both active power and power transfer rate are the minimum at $\lambda = 0$. Despite a decrease in the input power factor, both active power and power transfer rate reach their maximum at $\lambda = 0.9$. The matching circuit designed by (15) provides better active power and power

transfer rate performance for Type I, while the circuit designed by (14) performs better for Type II and III.

Note that for Type I, the input power factor reaches a maximum of 91.4% at $\lambda = 0$, while the active power and power transfer rate are only 1.17 mW and 9.3%, respectively. However, as λ increases to 0.9, the active power and power transfer rate rise to 1.80 mW and 18.5%, respectively, while the input power factor decreases 6.8%. For Type II and III, we obtain the maximum active powers of 0.95 mW and 0.61 mW at $\lambda = 0.9$, respectively. These represent improvements of 0.13 mW and 0.20 mW when no matching circuit is employed, respectively. The power transfer rates at $\lambda = 0.9$ are 9.5% and 10.1% for Type II and III, respectively, representing improvements of 1.4% and 4.2% compared to those at $\lambda = 0$.

Figure 8a–c illustrates the input power factors in Δf_e, Figure 8d–f shows the active powers delivered to the JHT, and Figure 8g–i shows the power transfer rates to the JHT. They are calculated with 1 V_{rms} input voltage. The input power factor decreases with increasing λ and it becomes the maximum at $\lambda = 0$, while the active power becomes the minimum. However, the maximum active power is achieved at $\lambda = 0.9$ for Type I and III and at $\lambda = 0.8$ for Type II, while input power factor is reduced. The maximum power transfer rate occurs at $\lambda = 0.9$ and the minimum at $\lambda = 0$ for all JHTs.

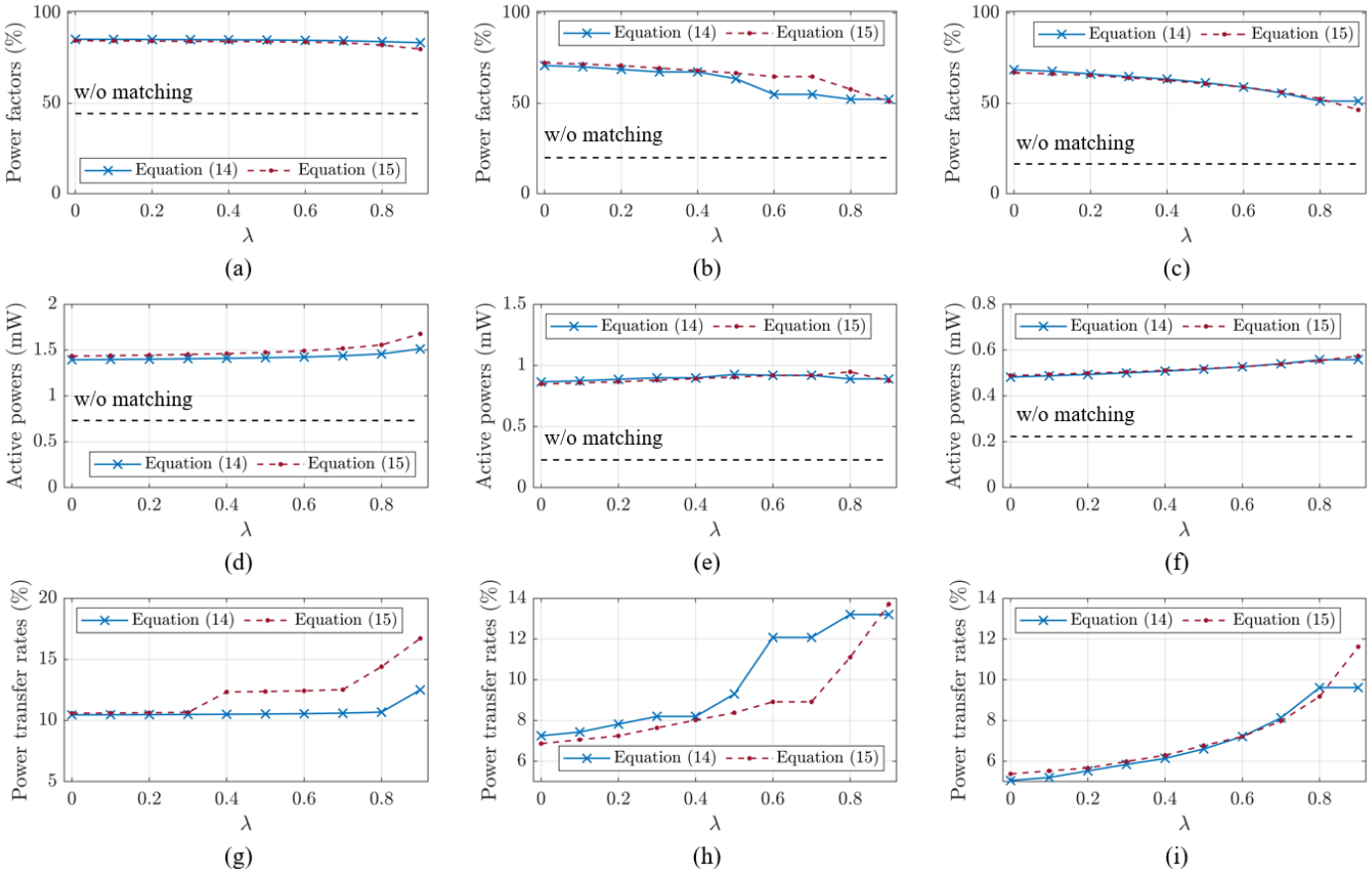


Figure 8. Changes (Type I, Type II and Type III) according to λ in the Δf_e for Case I: (**a–c**) the averages of input power factor, (**d–f**) the averages of active power delivered to the JHT and (**g–i**) the averages of power transfer rate to the JHT.

The objective function (15) yields better active power and power transfer rate performance than that with (14). Table 4 summarizes the performance of the three JHT types in terms of active power and power transfer rate across different λ values and frequency bands in Case I.

Table 4. Summary of average active power (in mW) and average power transfer rate (in %) in Case I.

Band	λ	Type I		Type II		Type III	
		Active Power	Power Transfer Rate	Active Power	Power Transfer Rate	Active Power	Power Transfer Rate
Δf_n	0.0	1.17	9.3	0.82	8.1	0.41	5.9
	0.9	1.80	18.5	0.95	9.5	0.61	10.1
Δf_e	0.0	1.43	10.5	0.84	6.8	0.48	5.3
	0.9	1.67	16.7	0.95	11.1	0.57	11.6

Figures A2 and A3 in Appendix D show the frequency response obtained using simulation program with integrated circuit emphasis (SPICE) within the Δf_n and Δf_e, respectively, for the three JHTs in Case I. Note that the values of L and C_m in the matching circuit are determined using $\lambda = 0.9$. The impedance matching circuit enhances the input power factors as well as the active powers delivered to the JHT across most frequencies in Δf_n. Similarly, the power factors and active powers improve across most frequencies in Δf_e.

3.3. Evaluation of the Impedance Matching Circuit in Case II

This section analyzes the performance of the impedance matching circuit for the three JHT types under Case II. Table A4 in Appendix E provides the optimized values of L and C_m, determined using the two objective functions across Δf_n and Δf_e for varying λ. Figure 9a–c displays the average input power factors over Δf_n, while Figure 9d–f shows the corresponding average active powers delivered to the JHTs. Figure 9g–i presents the corresponding averages of power transfer rate to the JHT. They are obtained by 1 V_{rms} input voltage.

For all JHTs, the input power factor decreases as λ increases and becomes maximum at $\lambda = 0$, while both the active power and power transfer rate are minimum. The maximum active power and power transfer rate are obtained at $\lambda = 0.9$, even though the input power factor is reduced. The circuit designed by (15) provides better active power and power transfer rate performance in for Type I and II, while the circuit designed by (14) performs better for Type III.

The input power factor of Type I reaches the maximum 88.0% at $\lambda = 0$, whereas the active power becomes the minimum 1.35 mW. At $\lambda = 0.9$, the input power factor drops by 3.3% to 84.7%, while the active power increases to the maximum 1.80 mW, being 1.37 mW higher than obtained without the matching circuit. The power transfer rate is 19.1%, representing 7.2% improvement to that with $\lambda = 0$. The active powers of Type II and III are 0.91 mW and 0.58 mW at $\lambda = 0.9$, respectively. They have improvements of 0.85 mW and 0.53 mW when no matching circuit is employed. The power transfer rates are 10.4% and 9.3%, showing 3.5% and 2.9% increases over those at $\lambda = 0$.

Figure 10a–c illustrates the average input power factors over Δf_e, and Figure 10d–f shows the average active powers delivered to the JHTs. Figure 10g–i presents the averages of power transfer rate to the JHT. They are obtained by 1 V_{rms} input voltage. For Type I, the design by (15) yields better active power and power transfer rate performance, whereas both objective functions result in similar performance for Type II. However, the design by (14) shows better performance for Type III. For all JHTs, the input power factor decreases as λ increases and becomes maximum at $\lambda = 0$, while both the active power and power transfer rate are minimum. The maximum active power and power transfer rate are obtained at $\lambda = 0.9$, even though the input power factor is reduced. Table 5 summarizes the performance of the three JHT types in terms of active power and power transfer rate across different λ values and frequency bands in Case II.

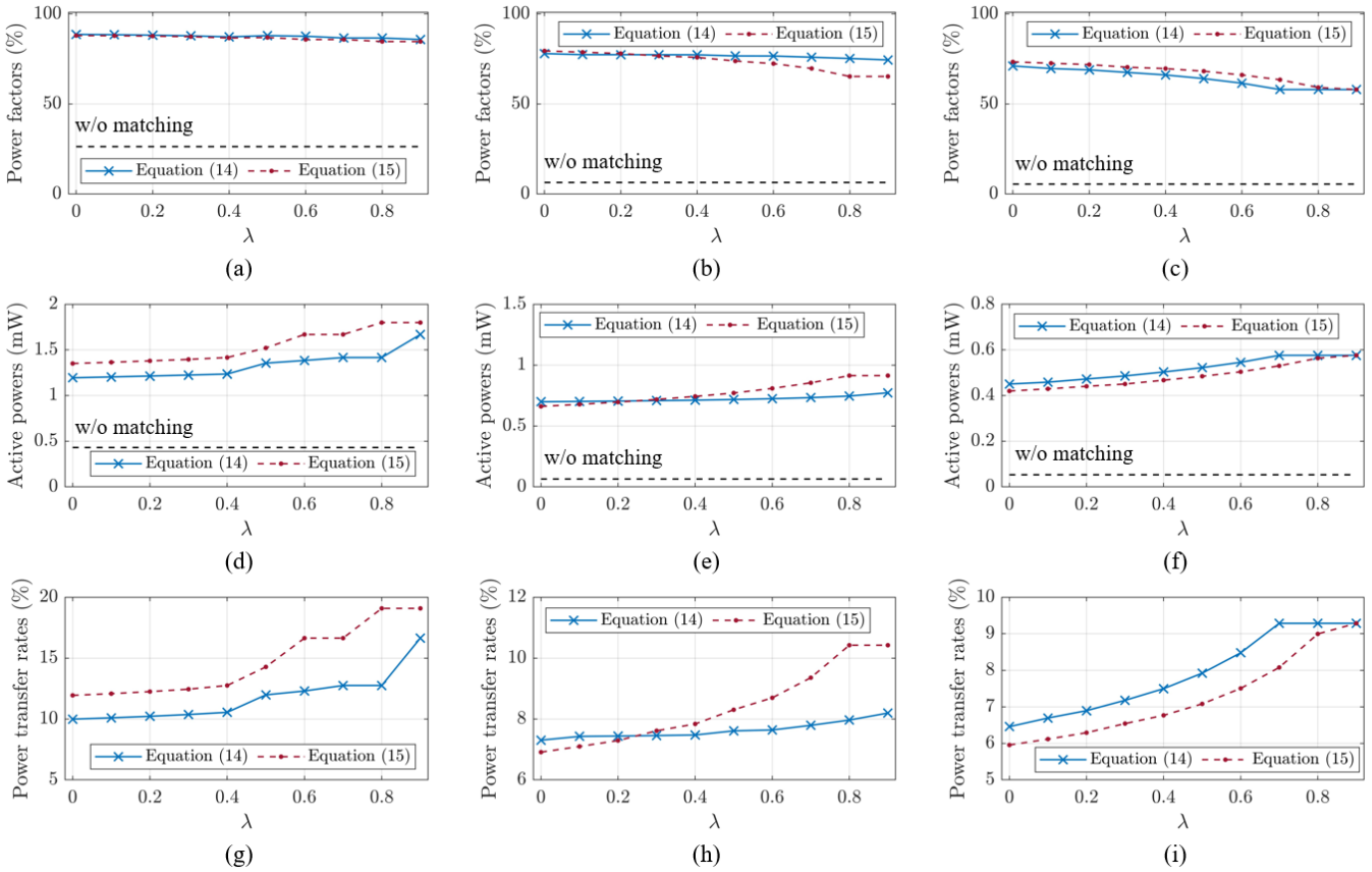


Figure 9. Changes (Type I, Type II and Type III) according to λ in the Δf_n for Case II: (**a**–**c**) the averages of input power factor, (**d**–**f**) the averages of active power delivered to the JHT and (**g**–**i**) the averages of power transfer rate to the JHT.

Table 5. Summary of average active power (in mW) and average power transfer rate (in %) in Case II.

Band	λ	Type I		Type II		Type III	
		Active Power	Power Transfer Rate	Active Power	Power Transfer Rate	Active Power	Power Transfer Rate
Δf_n	0.0	1.35	11.9	0.69	6.9	0.45	6.4
	0.9	1.80	19.1	0.91	10.4	0.58	9.3
Δf_e	0.0	1.53	12.9	0.81	7.5	0.48	5.5
	0.9	1.79	27.8	0.84	13.7	0.50	13.0

Figure A4 in Appendix E presents the frequency response obtained using SPICE within Δf_n for the three JHTs in Case II. Note that the values of L and C_m in the impedance matching circuit are determined with $\lambda = 0.9$. In Figure A4a–c, the input power factors for all JHTs increase across most frequencies compared to the case without impedance matching. The designed impedance matching circuit significantly enhances power efficiency, which is otherwise extremely low. Furthermore, Figure A4d–f demonstrates that the impedance matching circuit significantly enhances the active power. Figure A5 shows the frequency response within Δf_e for the three JHTs in Case II. The designed circuit continues to improve power efficiency across most frequencies.

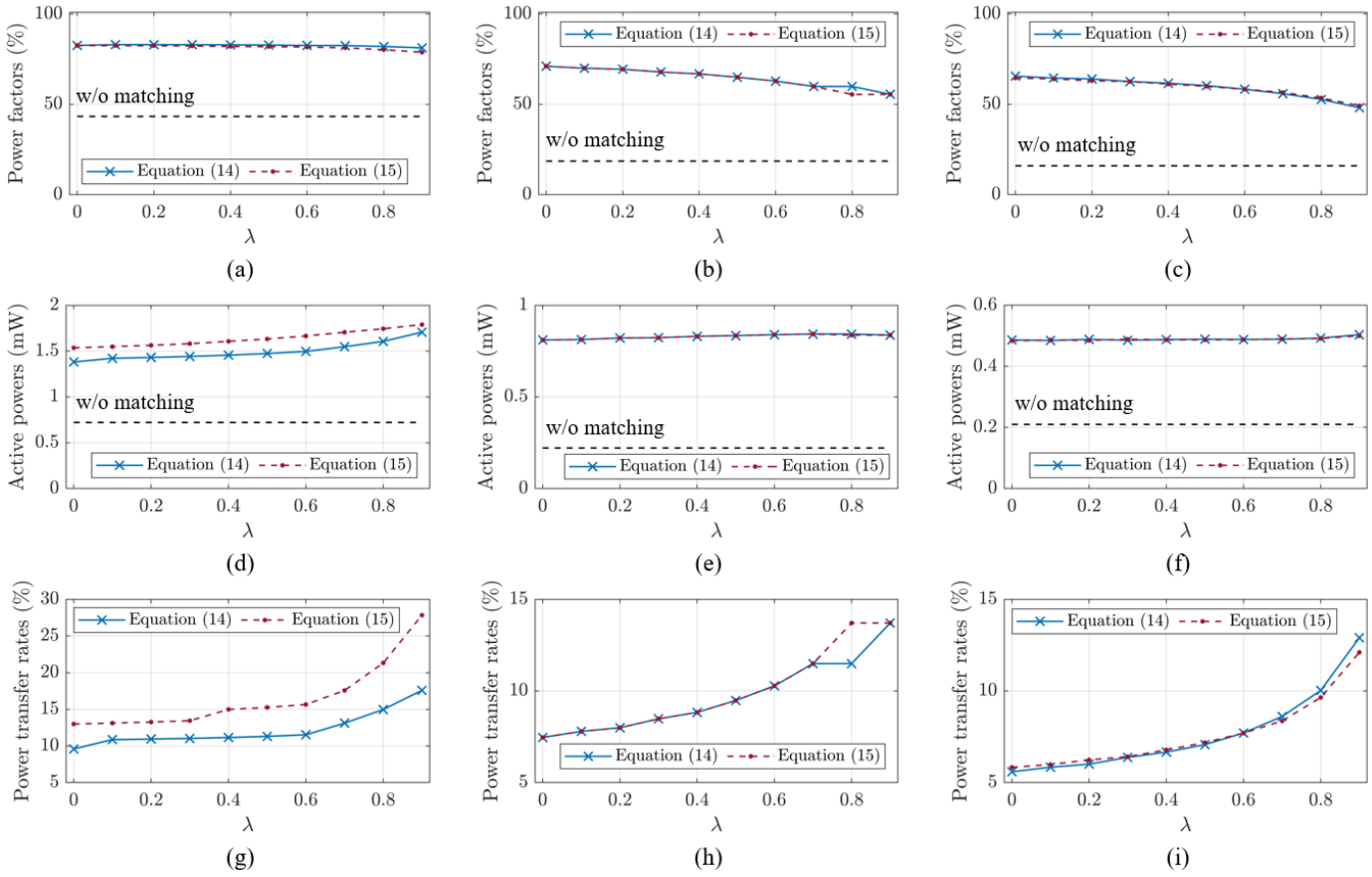


Figure 10. Changes (Type I, Type II and Type III) according to λ in the Δf_e for Case II: (**a**–**c**) the averages of input power factor, (**d**–**f**) the averages of active power delivered to the JHT and (**g**–**i**) the averages of power transfer rate to the JHT.

4. Experimental Results

To validate the proposed matching circuit, we perform an experiment by adopting the Butterworth–Van Dyke (BVD) equivalent circuit model for JHT [10,11]. The BVD circuit model consists of one capacitor in parallel with two RLC branches in Figure 11a.

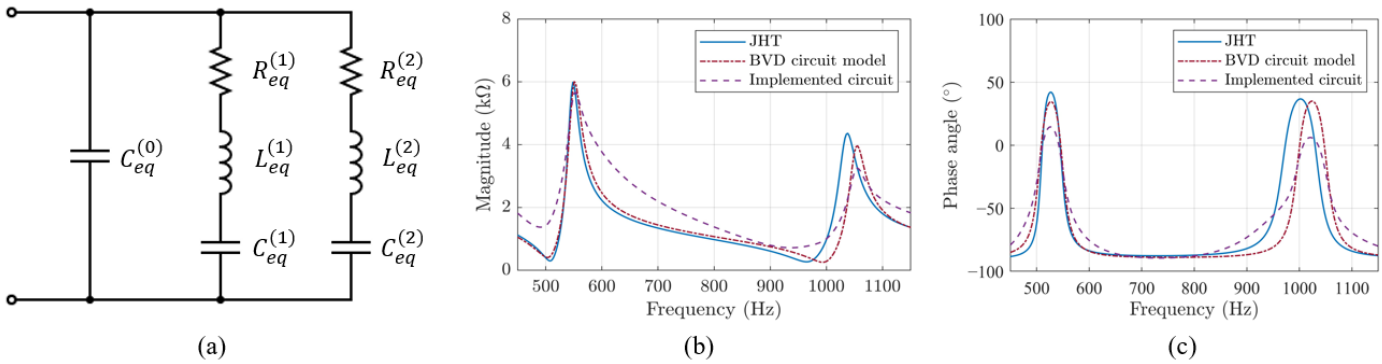


Figure 11. (**a**) BVD circuit diagram and its (**b**) magnitude and (**c**) phase responses.

We choose Type III JHT and estimate its RLC circuit component values by the PSO algorithm. The obtained parameters are $C_{eq}^{(0)} = 160$ nF, $R_{eq}^{(1)} = 430\ \Omega$, $L_{eq}^{(1)} = 300$ mH, $C_{eq}^{(1)} = 33$ nF, $R_{eq}^{(2)} = 270\ \Omega$, $L_{eq}^{(2)} = 150$ mH and $C_{eq}^{(2)} = 17.2$ nF. The impedance characteristics of the BVD circuit and their close matching with the JHT are shown in Figure 11b,c.

By using 3 m coaxial cable we design the matching circuit for Δf_n band of the BVD circuit model. The cable parameters are obtained by measuring impedance spectra at one end of the cable while leaving the other end open [12]. The extracted per-unit-length values are $R_c = 0.096\ \Omega$, $L_c = 351$ nH, $C_c = 10.3$ nF and $G_c = 111$ nS. Using these parameters, we simulate the impedance characteristics of the BVD equivalent circuit connected with the 3 m cable. The simulated impedance shown in Figure 12 closely matches the measured results, confirming that the model accurately represents the actual system behavior. Then, the matching circuits for Case I and II are designed by using $\lambda = 0.7$, at which maximum average active power is delivered to the JHT. The optimal circuit component values are obtained as $L = 512$ mH and $C_m = 498$ nF for Case I, and $L = 496$ mH and $C_m = 523$ nF for Case II. Figure 13 shows estimated input power factor and load active power with the designed matching circuit. Note that the frequency responses Case I and II are similar because a short cable of 3 m is used.

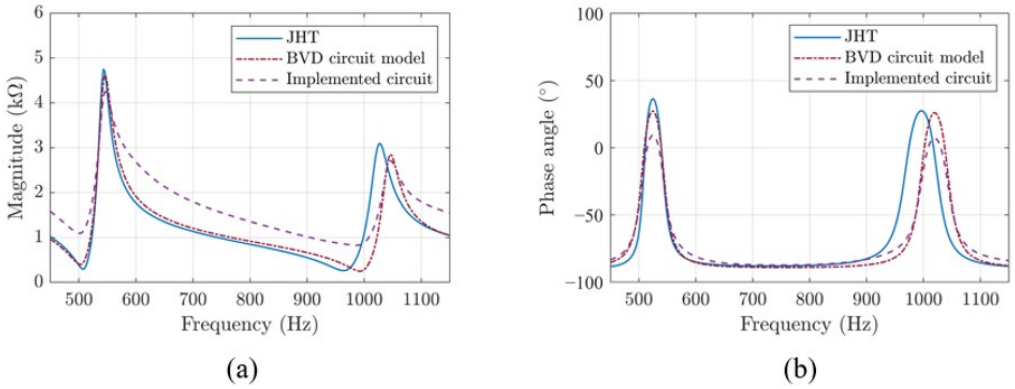


Figure 12. (**a**) Magnitude and (**b**) phase responses of overall circuit system including a 3 m cable.

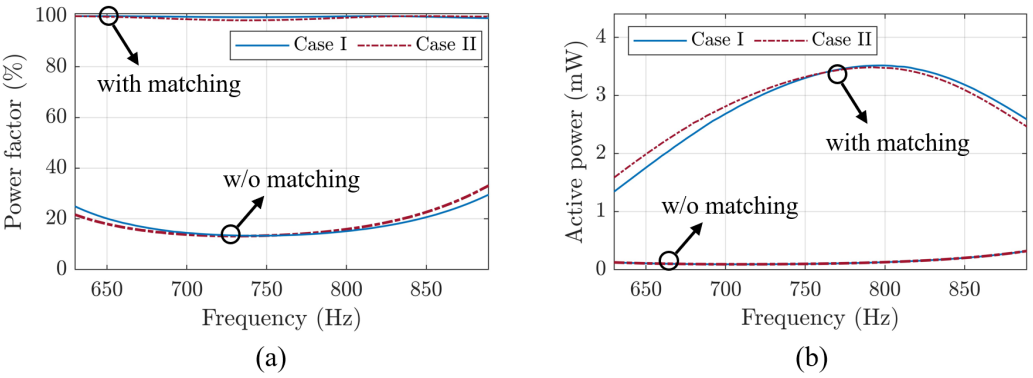


Figure 13. Estimated (**a**) input power factors and (**b**) active powers delivered to the JHT.

For simplicity, we only consider Case I and implement the matching circuit by using common $L = 500$ mH and $C_m = 500$ nF components, which are not optimum. Figure 14 shows the experimental setup along with the implemented BVD and matching circuits. By sweeping 1 V_{rms} sinusoidal signal over Δf_n band, we measure volatages of the circuit system. Then, input power factor and load active power are calculated with the measured impedances, which are shown in Figure 15. We obtain a 91.4% average input power factor, which is 73.2% higher than that of no matching circuit employed. Additionally, we obtain an increased average active power of 2.15 mW, which implies a 2.03 mW improvement when no matching circuit is employed.

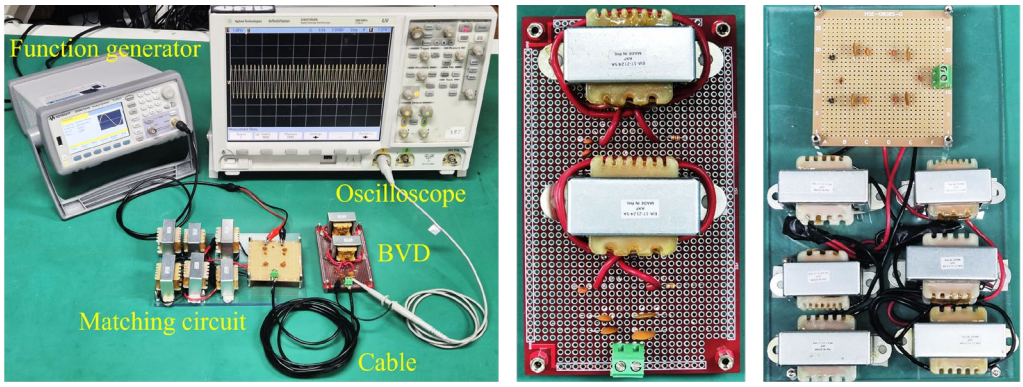


Figure 14. (**a**) Experimental setup, (**b**) implemented BVD circuit and (**c**) impedance matching circuit.

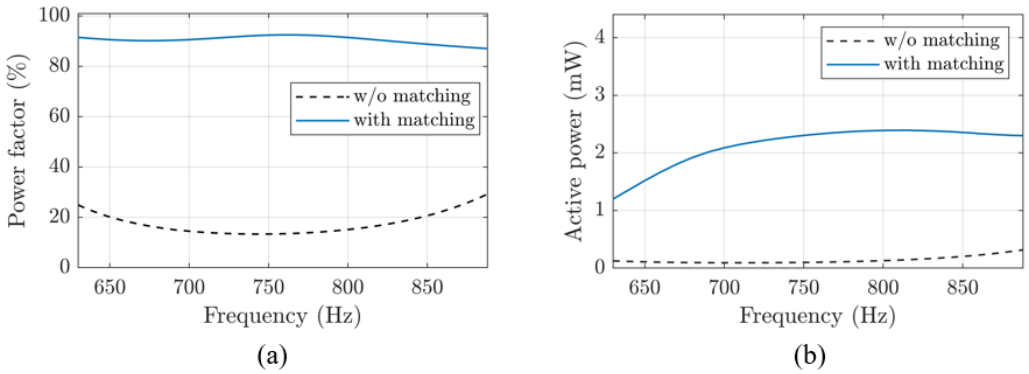


Figure 15. Measured (**a**) input power factors and (**b**) load active powers delivered to the JHT.

5. Conclusions

In this study, we proposed a design scheme for impedance matching circuit of a dual resonance to improve power transfer efficiency of the JHT. The design scheme utilizes equivalent driving power circuit system including minimal matching circuit and object function to maximize both input and load power factors. By considering three JHTs, two power driving systems and two frequency bands, we proved that the proposed matching circuit can achieve significant improvement of power transfer efficiency by choosing appropriate parameters for input and load power factors. Experimental results using equivalent JHT circuit model show that input power factor increases by 73.2%, while the active power delivered to the JHT increases by 2.03 mW with 1 V_{rms} input voltage.

We showed that the proposed matching circuit improves power transfer efficiency. However, the circuit based on dual resonance has limitation of maintaining consistent performance over a wide frequency band. Accordingly, this limitation suggests that extending the matching design beyond dual resonance may improve power transfer performance, which could be promising directions for future work.

Author Contributions: Conceptualization, K.L., C.H.L. and J.L.; methodology, K.L. and C.H.L.; investigation, K.L., H.H.Y., Y.J. and J.L.; data curation, K.L., H.H.Y. and Y.J.; writing—original draft preparation, K.L.; writing—review and editing, C.H.L. All authors have read and agreed to the published version of the manuscript.

Funding: This work was supported by the Korea Research Institute for defense Technology planning and advancement (KRIT)—Grant funded by Defense Acquisition Program Administration (DAPA) (KRIT-CT-23-026, Integrated Underwater Surveillance Research Center for Adapting Future Technologies).

Data Availability Statement: The original contributions presented in this study are included in the article. Further inquiries can be directed to the corresponding author.

Conflicts of Interest: The authors declare no conflicts of interest.

Abbreviations

The following abbreviations are used in this manuscript:

JHT	Janus Helmholtz Transducer
TVR	Transmission Voltage Response
KVL	Kirchhoff's Voltage Law'
PSO	Particle Swarm Optimization
SPICE	Simulation Program with Integrated Circuit Emphasis
BVD	Butterworth–Van Dyke

Appendix A

$$I_{1,1} = V_{in} / \left(R_{int} + Z_L - Z_L^2 / \left(Z_L + Z_C - Z_C^2 / \left(2Z_C + 2Z_{Cm} - Z_C^2 / \left(Z_L + Z_C - Z_L^2 / \left(Z_L + Z_{sc} + Z_{pc} - Z_{pc}^2 / (Z_{pc} + Z_l) \right) \right) \right) \right) \right) \quad \text{(A1)}$$

$$I_{1,2} = I_{1,1} Z_L / \left(Z_L + Z_C - Z_C^2 / \left(2Z_C + 2Z_{Cm} - Z_C^2 / \left(Z_L + Z_C - Z_L^2 / \left(Z_L + Z_{sc} + Z_{pc} - Z_{pc}^2 / (Z_{pc} + Z_l) \right) \right) \right) \right) \quad \text{(A2)}$$

$$I_{1,3} = I_{1,2} Z_C / \left(2Z_C + 2Z_{Cm} - Z_C^2 / \left(Z_L + Z_C - Z_L^2 / \left(Z_L + Z_{sc} + Z_{pc} - Z_{pc}^2 / (Z_{pc} + Z_l) \right) \right) \right) \quad \text{(A3)}$$

$$I_{1,4} = I_{1,3} Z_C / \left(Z_L + Z_C - Z_L^2 / \left(Z_L + Z_{sc} + Z_{pc} - Z_{pc}^2 / (Z_{pc} + Z_l) \right) \right) \quad \text{(A4)}$$

$$I_{1,5} = I_{1,4} Z_L / \left(Z_L + Z_{sc} + Z_{pc} - Z_{pc}^2 / (Z_{pc} + Z_l) \right) \quad \text{(A5)}$$

$$I_{1,6} = I_{1,5} Z_{pc} / (Z_{pc} + Z_l) \quad \text{(A6)}$$

$$I_{2,1} = V_{s,2} / \left(Z_{s,2} + Z_{sc} + Z_{pc} - Z_{pc}^2 / \left(Z_{pc} + Z_L - Z_L^2 / \left(Z_L + Z_C - Z_C^2 / \left(2Z_L + 2Z_C - Z_C^2 / \left(Z_L + Z_C - Z_L^2 / (Z_L + Z_l) \right) \right) \right) \right) \right) \quad \text{(A7)}$$

$$I_{2,2} = I_{2,1} Z_{pc} / \left(Z_{pc} + Z_L - Z_L^2 / \left(Z_L + Z_C - Z_C^2 / \left(2Z_L + 2Z_C - Z_C^2 / \left(Z_L + Z_C - Z_L^2 / (Z_L + Z_l) \right) \right) \right) \right) \quad \text{(A8)}$$

$$I_{2,3} = I_{2,2} Z_L / \left(Z_L + Z_C - Z_C^2 / \left(2Z_L + 2Z_C - Z_C^2 / \left(Z_L + Z_C - Z_L^2 / (Z_L + Z_l) \right) \right) \right) \quad \text{(A9)}$$

$$I_{2,4} = I_{2,3} Z_C / \left(2Z_L + 2Z_C - Z_C^2 / \left(Z_L + Z_C - Z_L^2 / (Z_L + Z_l) \right) \right) \quad \text{(A10)}$$

$$I_{2,5} = I_{2,4} Z_C / \left(Z_L + Z_C - Z_L^2 / (Z_L + Z_l) \right) \quad \text{(A11)}$$

$$I_{2,6} = I_{2,5} Z_L / (Z_L + Z_l) \quad \text{(A12)}$$

Appendix B

The impedance $Z_{s,2}$ in Case II includes both the voltage source and the cable. Thus, the input current $I_{i,2}$ can be expressed by incorporating $R_{s,2}(f)$ and $X_{s,2}(f)$ as follows:

$$I_{i,2}(\phi,\ f) = \frac{V_{s,2}(f)}{R_{s,2}(f) + R_{i,2}(\phi,\ f) + j(X_{s,2}(f) + X_{i,2}(\phi,\ f))} \quad \text{(A13)}$$

Using $I_{i,2}(\phi,\ f)$ in (A13), the input active power $P_{a,2}(\phi,\ f)$ can be expanded as follows:

$$P_{a,2}(\phi,\ f) = |I_{i,2}(\phi,\ f)|^2 R_{i,2}(\phi,f) = \frac{|V_{s,2}(f)|^2 R_{i,2}(\phi,f)}{(R_{s,2}(f) + R_{i,2}(\phi,f))^2 + (X_{s,2}(f) + X_{i,2}(\phi,\ f))^2} \tag{A14}$$

We can define input power factor $\eta_2(\phi,\ f)$ in Case II by evaluating the input power $P_{i,2}(\phi,\ f)$ expressed as follows:

$$P_{i,2}(\phi,\ f) = |I_{i,2}(\phi,\ f)|^2 \sqrt{R_{i,2}^2(\phi,f) + X_{i,2}^2(\phi,\ f)} \tag{A15}$$

Then, the $\eta_2(\phi,\ f)$ becomes as follows:

$$\eta_2(\phi,\ f) = \frac{P_{a,2}(\phi,\ f)}{P_{i,2}(\phi,\ f)} = \frac{1}{\sqrt{1 + (X_{i,2}(\phi,\ f)/R_{i,2}(\phi,f))^2}} \tag{A16}$$

Note that $\eta_2(\phi,\ f)$ is normalized as $0 \leq \eta_2(\phi,\ f) \leq 1$. We can express load power factor $\psi(f)$ in Case II by using the active power $Q_{a,2}(f)$ and total load power $Q_{l,2}(f)$ expressed as follows:

$$Q_{a,2}(\phi,f) = \left|I_{l,2}(\phi,f)\right|^2 R_l(f) \tag{A17}$$

$$Q_{l,2}(\phi,f) = \left|I_{l,2}(\phi,f)\right|^2 \sqrt{R_l^2(f) + X_l^2(f)} \tag{A18}$$

Then the $\psi(f)$ becomes the following:

$$\psi(f) = \frac{Q_{a,2}(f)}{Q_{l,2}(f)} = \frac{1}{\sqrt{1 + (X_l(f)/R_l(f))^2}} \tag{A19}$$

Appendix C

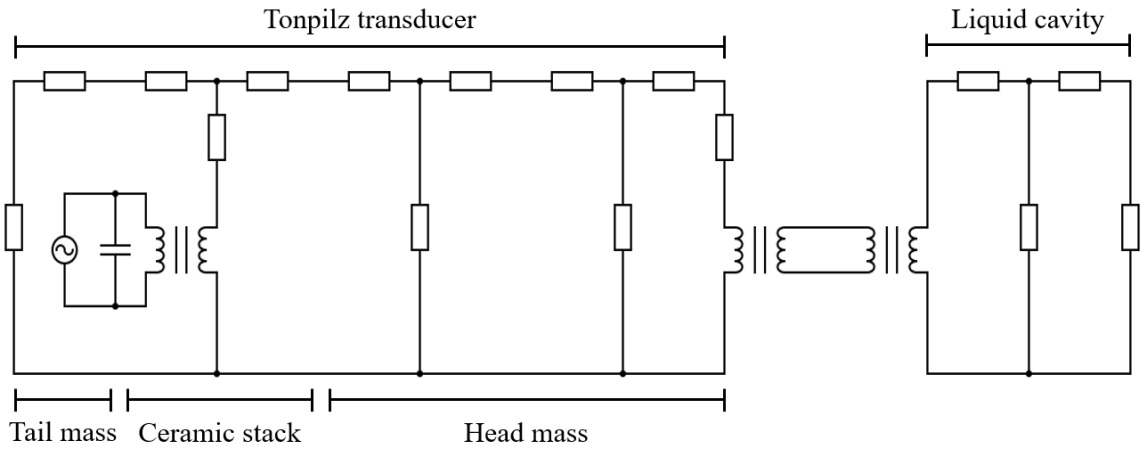


Figure A1. The DPM for the design and impedance characterization of the JHT.

Table A1. Material properties of the JHT [8].

Material Properties	Unit	Value
Elastic modulus of the piezoelectric disc	m^2/N	15.5×10^{-12}
Density of the tail mass	kg/m^3	4510
Young's modulus of the tail mass	pa	110×10^9
Density of the head mass	kg/m^3	4500
Young's modulus of the head mass	pa	116×10^9
Young's modulus of the cylindrical housing	pa	70×10^9

Table A2. Electrical parameters of the cable [12].

Parameters	Unit	Value
Resistance (R_c)	Ω	107×10^{-3}
Inductance (L_c)	H	321×10^{-9}
Capacitance (C_c)	F	98.7×10^{-12}
Conductance (G_c)	S	12.8×10^{-9}

Appendix D

Table A3. L (in mH) and C_m (in nF) of the impedance matching circuit in Case I.

Band	λ	Type I				Type II				Type III			
		Equation (14)		Equation (15)		Equation (14)		Equation (15)		Equation (14)		Equation (15)	
		L	C_m	L	C_m	L	C_m	L	C_m	L	C_m	L	C_m
Δf_n	0.0	7	1778	7	1704	49	1544	47	1541	44	2013	41	2178
	0.1	7	1769	7	1689	48	1506	47	1537	45	1949	42	2120
	0.2	7	1759	7	1671	48	1500	47	1532	47	1879	43	2056
	0.3	7	1747	7	1648	48	1492	47	1526	49	1800	45	1984
	0.4	7	1730	8	1619	49	1483	47	1519	51	1710	46	1903
	0.5	7	1708	8	1578	49	1471	48	1510	54	1607	49	1809
	0.6	7	1676	8	1522	50	1454	48	1498	58	1484	51	1698
	0.7	8	1623	9	1443	50	1430	49	1480	64	1332	55	1561
	0.8	8	1525	9	1323	52	1387	50	1452	73	1130	62	1380
	0.9	9	1317	11	1118	57	1270	52	1386	73	1130	62	1380
Δf_e	0.0	8	1834	8	1769	44	2063	42	2187	39	3022	41	2895
	0.1	8	1830	8	1762	45	1989	43	2121	40	2922	42	2809
	0.2	8	1824	8	1752	47	1907	44	2048	42	2811	43	2715
	0.3	8	1817	8	1741	49	1815	46	1966	44	2689	45	2611
	0.4	8	1809	9	1728	49	1815	48	1873	46	2551	47	2494
	0.5	8	1799	9	1709	55	1587	50	1764	49	2392	50	2360
	0.6	8	1786	9	1684	74	877	53	1635	53	2206	53	2203
	0.7	8	1766	9	1645	74	877	53	1635	59	1977	58	2010
	0.8	8	1732	10	1573	84	758	66	1241	69	1678	66	1758
	0.9	9	1651	11	1389	84	758	89	716	69	1678	83	1380

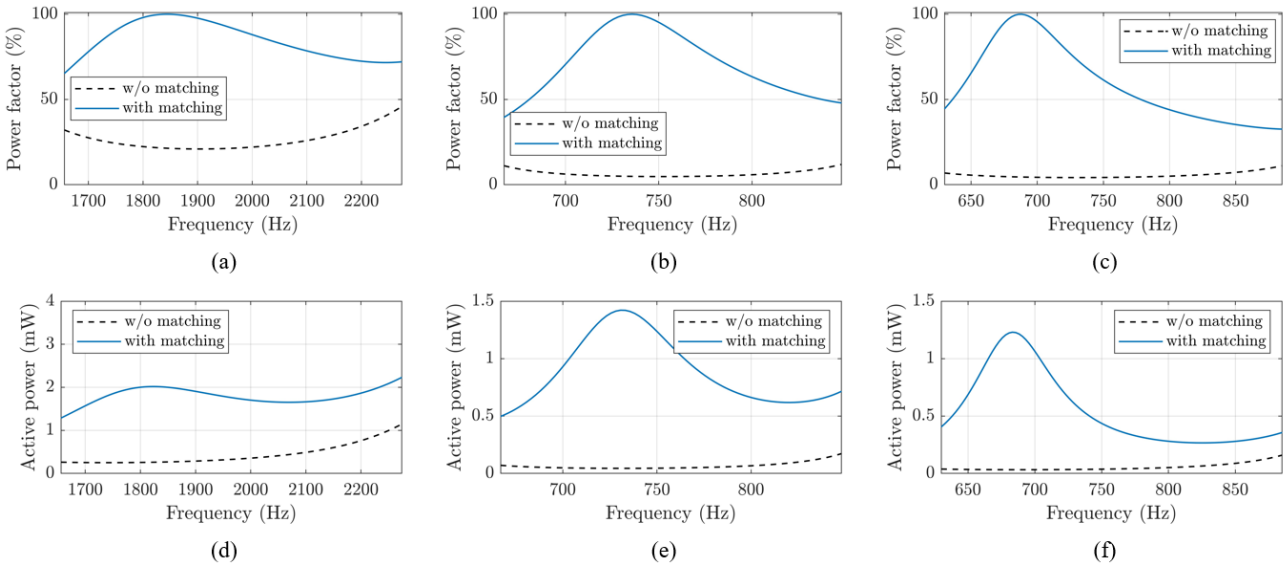


Figure A2. Frequency response (Δf_n) of Type I, Type II and Type III for the three JHTs in Case I: (**a**–**c**) input power factors and (**d**–**f**) load active powers.

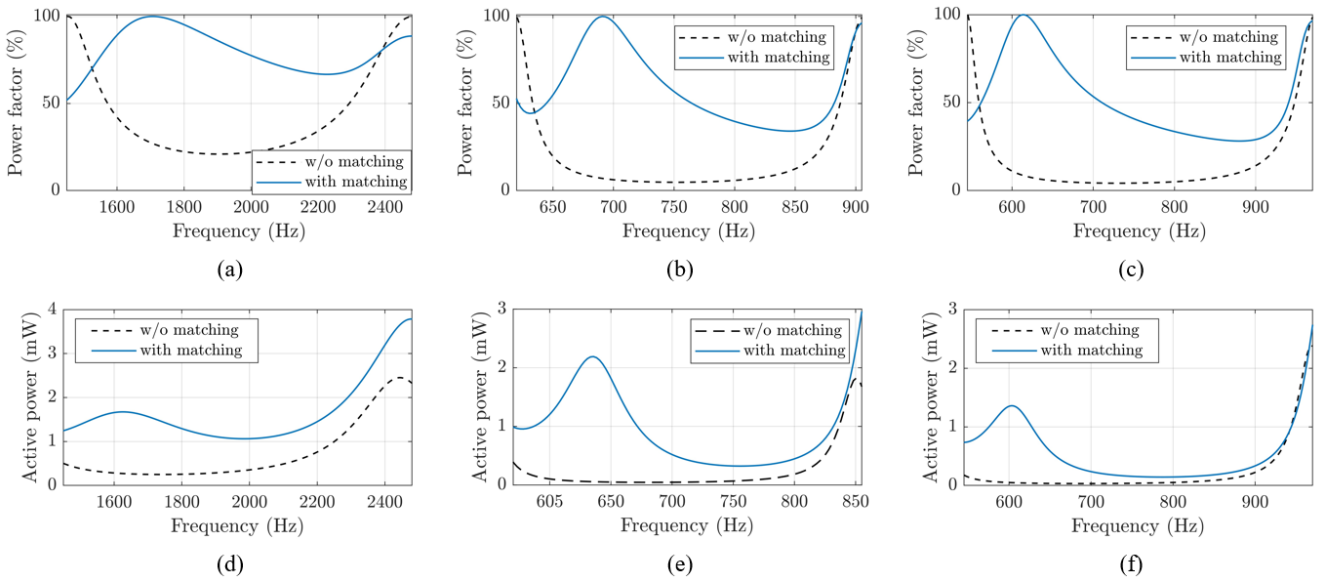


Figure A3. Frequency response (Δf_e) of Type I, Type II and Type III for the three JHTs in Case I: (**a**–**c**) input power factors and (**d**–**f**) load active powers.

Appendix E

Table A4. L (in mH) and C_m (in nF) of the impedance matching circuit in Case II.

Band	λ	Type I				Type II				Type III			
		Equation (14)		Equation (15)		Equation (14)		Equation (15)		Equation (14)		Equation (15)	
		L	C_m	L	C_m	L	C_m	L	C_m	L	C_m	L	C_m
Δf_n	0.0	7	1295	8	1190	45	1491	43	1578	45	1606	42	1732
	0.1	7	1279	8	1173	46	1485	44	1539	47	1561	43	1691
	0.2	7	1261	8	1153	46	1479	45	1497	48	1512	44	1646
	0.3	7	1240	8	1130	46	1471	47	1449	50	1455	46	1595
	0.4	7	1215	8	1096	46	1462	48	1395	52	1391	47	1537
	0.5	8	1185	9	1070	47	1450	51	1332	55	1315	49	1470
	0.6	8	1147	10	974	47	1436	53	1255	59	1223	52	1389
	0.7	8	1096	10	974	48	1416	57	1158	65	1104	56	1287
	0.8	8	1096	11	890	49	1387	64	1025	65	1104	63	1147
	0.9	10	974	11	890	50	1332	64	1025	65	1104	65	1104
Δf_e	0.0	7	1358	9	1217	47	1547	47	1547	43	1962	45	1916
	0.1	8	1347	9	1201	49	1499	49	1499	45	1910	46	1869
	0.2	8	1334	9	1182	50	1445	50	1445	46	1852	48	1817
	0.3	8	1319	9	1160	53	1385	53	1385	49	1786	49	1759
	0.4	8	1300	10	1134	55	1315	55	1315	51	1712	52	1693
	0.5	8	1276	10	1103	59	1234	59	1234	54	1625	55	1617
	0.6	8	1245	10	1062	64	1134	64	1134	59	1522	59	1526
	0.7	9	1202	11	1007	72	1005	72	1005	66	1395	64	1414
	0.8	10	1135	13	924	72	1005	88	822	77	1231	74	1267
	0.9	11	1006	16	771	88	822	88	822	99	1023	93	1066

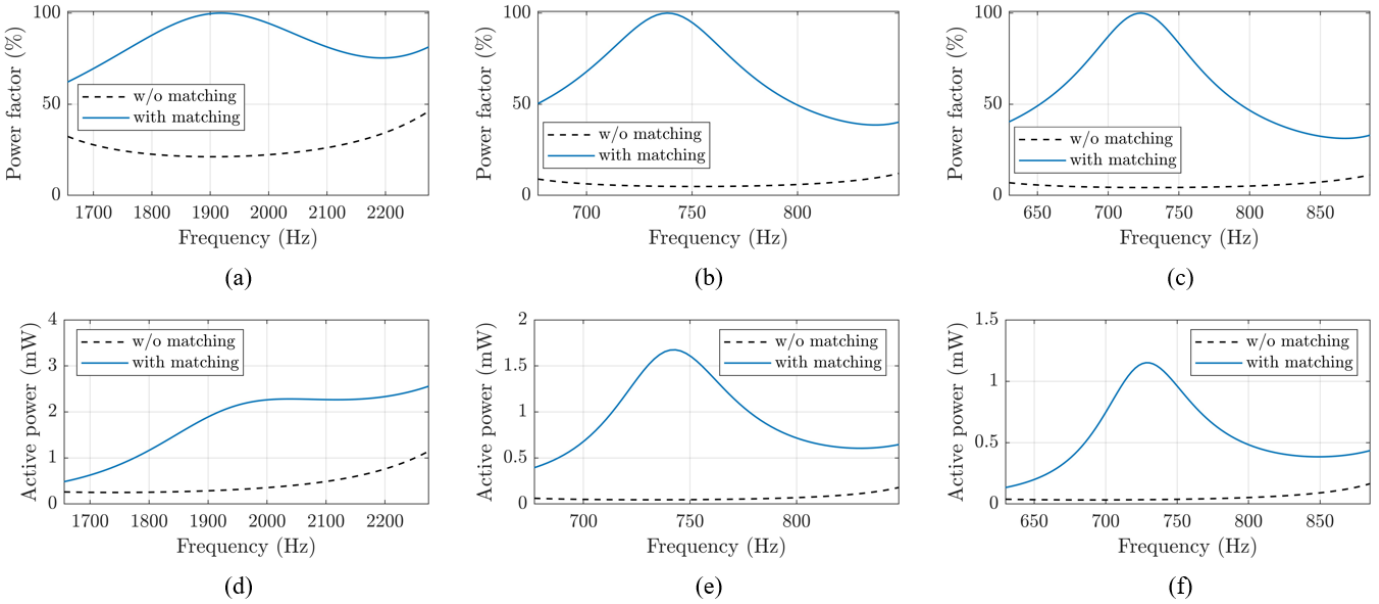


Figure A4. Frequency response (Δf_n) of Type I, Type II and Type III for the three JHTs in Case II: (**a**–**c**) input power factors and (**d**–**f**) load active powers.

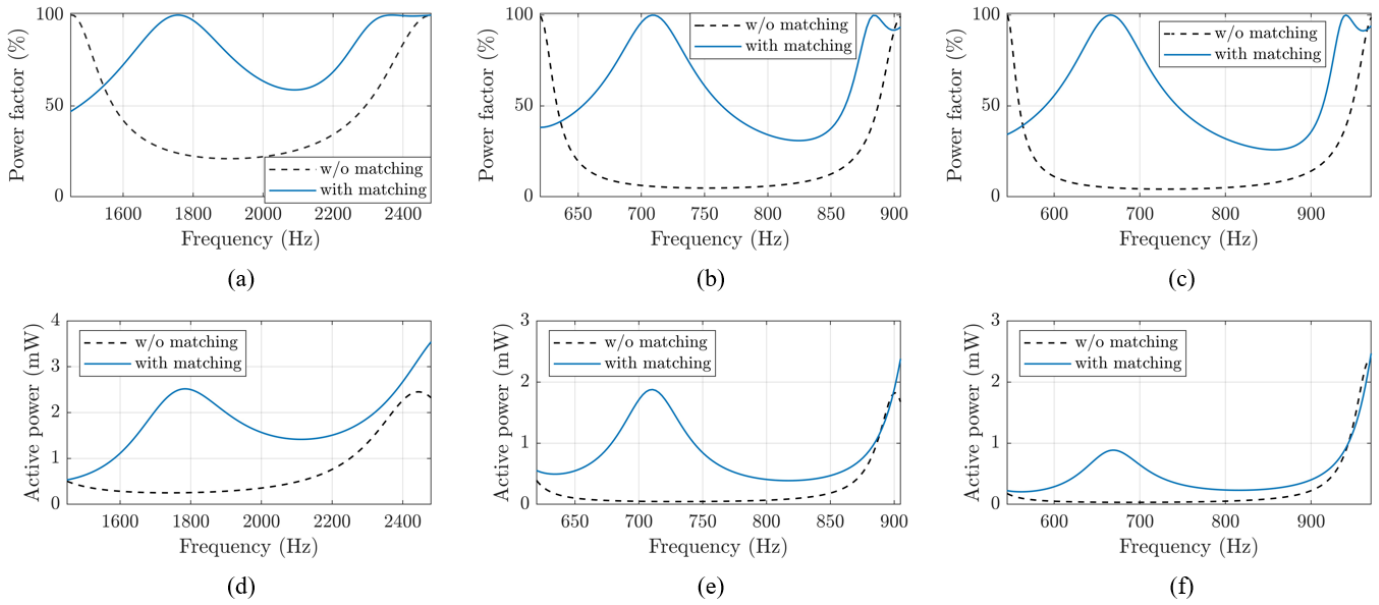


Figure A5. Frequency response (Δf_e) of Type I, Type II and Type III for the three JHTs in Case II: (**a**–**c**) input power factors and (**d**–**f**) load active powers.

References

1. Afzal, M.S.; Lim, Y.; Lee, S.; Yoon, H.; Roh, Y. Optimization and characterization of a wideband multimode Tonpilz transducer for underwater acoustical arrays. *Sens. Actuat A-Phys.* **2020**, *307*, 112001. [CrossRef]
2. Abdullah, Z.; Nix, S.; Raja, M.A.Z.; Zammer, A. Design of wideband Tonpilz transducer for underwater SONAR applications with finite element model. *Appl. Acoust.* **2021**, *183*, 108293. [CrossRef]
3. Pyo, S.; Afzal, M.S.; Lim, Y.; Lee, S.; Roh, Y. Design of a wideband Tonpilz transducer comprising non-uniform piezoceramic stacks with equivalent circuits. *Sensors* **2021**, *21*, 2680. [CrossRef] [PubMed]
4. Bian, J.; Wang, Y.; Liu, Z.; Shen, M.; Zhao, H.; Sun, Y.; Zhu, J. Ultra-wideband underwater acoustic transducer with a gradient impedance matching layer. *Appl. Acoust.* **2021**, *175*, 107789. [CrossRef]
5. Chen, W.; Ma, S.; Lai, X.; Wang, Z.; Zhao, H.; Zha, Q.; Chiu, Y.; Jin, Y. Design, fabrication, characterization, and simulation of AIN-based piezoelectric micromachined ultrasonic transducer for sonar imaging applications. *Micromachines* **2024**, *15*, 751.

6. Gall, Y.L.; Boucher, D.; Lurton, X.; Bruneau, A.M. A 300 Hz Janus-Helmholtz transducer for ocean acoustic tomography. In Proceedings of the OCEANS '93, Victoria, BC, Canada, 18–21 October 1993; pp. 278–281.
7. Zhang, Y. A longitudinal-bending fluid-cavity coupled broadband underwater acoustic transducer. In Proceedings of the 2020 15th Symposium on Piezoelectricity, Acoustic Waves and Device Applications, Zhengzhou, China, 16–19 April 2021; pp. 390–393.
8. Liu, W.; Mo, X.; Chai, Y.; Wu, T.; Pan, R. A distributed parameter model of the Janus-Helmholtz transducer. *JASA* **2024**, *25*, 681–694. [CrossRef] [PubMed]
9. Liu, W.; Mo, X.; Chai, Y.; Wu, T.; Zhang, X. Broadband Janus-Helmholtz transducer with various liquid cavity resonances. *Appl. Acoust.* **2024**, *221*, 110032. [CrossRef]
10. Lee, J.; Lee, B.; Baek, K. Estimation of equivalent circuit parameters of underwater acoustic piezoelectric transducer for matching network design of sonar transmitter. *J. KIMST* **2009**, *12*, 282–289.
11. Choi, J.; Mok, H. Simultaneous design of low-pass filter with impedance matching transformer for SONAR transducer using particle swarm optimization. *Energies* **2019**, *12*, 4646. [CrossRef]
12. Manoj, G.; Ramesh, R.; Kundukulam, S.O. Impedance matching network of passive coupler with coaxial cable for airborne sonar applications. *Adv. Mil. Technol.* **2023**, *18*, 49–66. [CrossRef]
13. Shin, C.; Lee, Y.; Ahn, B.; Yoon, H.; Kwon, B.; Kim, K.; Lee, J. Design and output control technique of sonar transmitter considering impedance variation of underwater acoustic transducer. *J. ASK* **2022**, *41*, 481–491.
14. Zhou, H.; Huang, S.H.; Li, W. Electrical impedance matching between piezoelectric transducer and power amplifier. *IEEE Sens. J.* **2020**, *20*, 14273–14281. [CrossRef]
15. Li, J.; Huang, W.; Shao, W.; Li, X.; Sen, Z.; Xu, J.; Shen, J.; Cui, Y. An electrical impedance matching method of dual-frequency transducers for ultrasound internal imaging. *Measurement* **2023**, *221*, 113413. [CrossRef]
16. Tian, W.; Wang, L.; Yu, J.; Lv, Y.; Zhang, S.; Xu, Q.; Gao, B. A hybrid impedance matching network for underwater acoustic transducers. *IEEE Trans. Power Electron.* **2023**, *38*, 7622–7632. [CrossRef]
17. Yu, J.; Tian, W.; Zhang, K.; Liao, S.; Xu, Q. An adaptive broadband active impedance matching network for underwater electroacoustic transduction system. *IEEE Trans. Ind. Electron.* **2023**, *70*, 5433–5443. [CrossRef]
18. Bevilacqua, A.; Mazzanti, A. Doubly-tuned transformer networks: A tutorial. *IEEE Trans. Circuits Syst. II* **2021**, *68*, 550–555. [CrossRef]
19. Bhagavatula, V.; Zhang, T.; Suvarna, A.R.; Rudell, J.C. An ultra-wideband IF millimeter-wave receiver with a 20 GHz channel bandwidth using gain-equalized transformers. *IEEE J. Solid-State Circuits* **2016**, *51*, 323–331. [CrossRef]
20. Poole, C.; Darwazeh, I. *Microwave Active Circuit Analysis and Design*, 1st ed.; Academic Press: Cambridge, MA, USA, 2015; pp. 51–87.
21. Irwin, J.D.; Nelms, R.M. *Engineering Circuit Analysis*, 10th ed.; John Wiley & Sons, Inc.: Hoboken, NJ, USA; pp. 102–140.
22. Mezura-Montes, E.; Coello Coello, C.A. Constraint-handling in nature-inspired numerical optimization: Past, present and future. *Swarm Evol. Comput.* **2011**, *1*, 173–194. [CrossRef]

Disclaimer/Publisher's Note: The statements, opinions and data contained in all publications are solely those of the individual author(s) and contributor(s) and not of MDPI and/or the editor(s). MDPI and/or the editor(s) disclaim responsibility for any injury to people or property resulting from any ideas, methods, instructions or products referred to in the content.